

Furrow Constriction in Animal Cell Cytokinesis

Hervé Turlier,^{†*} Basile Audoly,[‡] Jacques Prost,^{†§} and Jean-François Joanny[†]

[†]Physicochimie Curie (Centre National de la Recherche Scientifique-UMR168), Institut Curie, Section de Recherche, Paris, France; [‡]Institut Jean Le Rond d'Alembert (Centre National de la Recherche Scientifique-UMR7190), Université Pierre-et-Marie-Curie, Université Paris VI, Paris, France; and [§]École Supérieure de Physique et de Chimie Industrielles de la Ville de Paris-ParisTech, Paris, France

ABSTRACT Cytokinesis is the process of physical cleavage at the end of cell division; it proceeds by ingression of an actomyosin furrow at the equator of the cell. Its failure leads to multinucleated cells and is a possible cause of tumorigenesis. Here, we calculate the full dynamics of furrow ingression and predict cytokinesis completion above a well-defined threshold of equatorial contractility. The cortical actomyosin is identified as the main source of mechanical dissipation and active forces. Thereupon, we propose a viscous active nonlinear membrane theory of the cortex that explicitly includes actin turnover and where the active RhoA signal leads to an equatorial band of myosin overactivity. The resulting cortex deformation is calculated numerically, and reproduces well the features of cytokinesis such as cell shape and cortical flows toward the equator. Our theory gives a physical explanation of the independence of cytokinesis duration on cell size in embryos. It also predicts a critical role of turnover on the rate and success of furrow constriction. Scaling arguments allow for a simple interpretation of the numerical results and unveil the key mechanism that generates the threshold for cytokinesis completion: cytoplasmic incompressibility results in a competition between the furrow line tension and the cell poles' surface tension.

INTRODUCTION

Cytokinesis is one of the most striking hallmarks of cell division but its precise description and understanding have been challenging biologists and physicists for >50 years. Significant progress has been achieved during the last decade with advances in genomics, molecular biology, and imaging techniques, which allowed us to identify >100 proteins (1) implicated in this highly complex cellular process. Its tight regulation is as critical for cell division success as chromosome replication and separation: its failure leads generally to aberrant ploidy, which can ultimately cause cancer (2). The features and molecular processes involved in cytokinesis are remarkably similar among animal organisms (3), suggesting the existence of a common fundamental mechanism.

Mechanical engineers and physicists tried early to address the drastic cell deformation occurring during cytokinesis. Continuous elastic, viscous, analytical, and computational models of the entire cell surface have been proposed (4–8) to account for early experimental observations and force measurements performed on sea-urchin eggs (9). By contrast, most of the recent theoretical work is focused on the so-called contractile ring, based on coarse-grained descriptions (10–12) or microscopic models for motor-filament interactions (13,14). In our approach, the cell surface is viewed as a continuum, in the spirit of earlier work (4–6,8), but it is treated using recent active-gel models for actomyosin rheology (15,16). Adhesive forces have been proposed to contribute to furrow constriction in nonanimal

Dictyostelium discoideum cells (17). Here, we consider neither cell-cell nor cell-substrate adhesion. Our model would therefore be well adapted for cell lines dividing in suspension, such as eggs or leukocytes. Recent experimental studies have highlighted that tight regulation of the contractility at the cell poles is essential for cell shape stability (18,19). Here, we show that the contractility, but also the dissipation at cell poles, are limiting factors controlling primarily the constriction of the cleavage furrow.

MODEL

The actomyosin cortex: main source of active forces and dissipation

The cell is actively shaped by cytoskeleton elements, essentially the microtubules and the actomyosin cortex (20). Although an intact and functional actomyosin cortex is necessary for furrowing (21–23), it has been shown that microtubules need not be in contact with the cell surface for proper constriction (24). They therefore do not shape the cell surface directly, but are nevertheless responsible for positioning the cleavage furrow by delivering the biochemical signal that activates locally contractile forces in the cortex (25–27), as suggested by Rappaport's early experiments (28).

In animal cells, the typical plasma membrane tension is one order-of-magnitude smaller than the typical active tension developed by the actomyosin cortex (29). In addition, the plasma membrane does not prevent cell surface expansion, because several regulatory mechanisms ensure permanent plasma membrane surface availability, including disassembly of caveolae on shorter timescales (30) and membrane trafficking on longer timescales (31,32). The mechanical role of the plasma membrane can therefore be neglected in normal conditions. It has been proposed that abrupt detachments of plasma membrane from the cortex, called blebs, can act locally as cytoplasmic pressure valves in specific cells (18,19). However, their stochastic nature at the scale of the cell still challenges efficient modeling and we therefore restrict the application of our model to nonblebbing cells such as eggs and embryos.

The cytoplasm is squeezed toward polar regions by the furrow constriction, as reported in early experiments of Hiramoto (9). It can also be

Submitted September 10, 2013, and accepted for publication November 11, 2013.

*Correspondence: herve.turlier@polytechnique.org

Editor: Jochen Guck.

© 2014 by the Biophysical Society
0006-3495/14/01/0114/10 \$2.00

<http://dx.doi.org/10.1016/j.bpj.2013.11.014>



advected along the cortex by cortical flows. The cytoplasmic pressure associated with these flows has been measured to relax within a few seconds (33), whereas in cytokinesis, the cortical deformation occurs in several minutes. On this slower timescale, the response of the cytoplasm can therefore be captured by a uniform pressure. Viscous dissipation in the cytoplasm can be neglected, because it is generally much lower than the dissipation in the cortex, at least for cells <1 mm in size (see the [Supporting Material](#)).

A nonlinear visco-active membrane model for the acto-myosin cortex

The response of the acto-myosin cortex is well captured by the Maxwell viscoelastic model: elastic at short timescale, viscous at longer times. Because the elastic stress is released upon renewal of the layer, the viscoelastic relaxation time of the material must be smaller than the typical time for turnover. The latter has been found to be of the order of a few tens of seconds based on fluorescence recovery after photobleaching

(FRAP) experiments in polar and equatorial cortices (34–36). This is much shorter than the typical cytokinesis duration, which is in the range of 5–30 min. The cortex can therefore be viewed as a purely viscous fluid during constriction. Inertial effects are also completely negligible (37).

Given that the cortex is thin relative to the cell radius, the cortical layer is represented by a thin shell model (38). As long as the stress tangent to the cell surface remains tensile, no buckling occurs and one can ignore the small bending moments: this is the so-called membrane theory in mechanics (39) (not to be confused with the plasma membrane). We formulate here a visco-active membrane theory of the cortex and solve it numerically for large deformations.

We use a Lagrangian description (see the [Supporting Material](#)), which makes the numerical implementation easier. The reference configuration is an initial spherical shape (Fig. 1, t_0) that corresponds to the metaphase round cell (40). As suggested by observation, we assume that the cell remains axisymmetric (see Fig. S1 A and Movie S5 in the [Supporting Material](#)): a section plane ($\mathbf{e}_z, \mathbf{e}_r$) of the cell is shown in Fig. 1. The membrane tension is therefore a diagonal tensor (see the [Supporting Material](#)) in the curvilinear frame ($\mathbf{t}, \mathbf{e}_\phi$) (Fig. 1, t_0). It involves axial and azimuthal

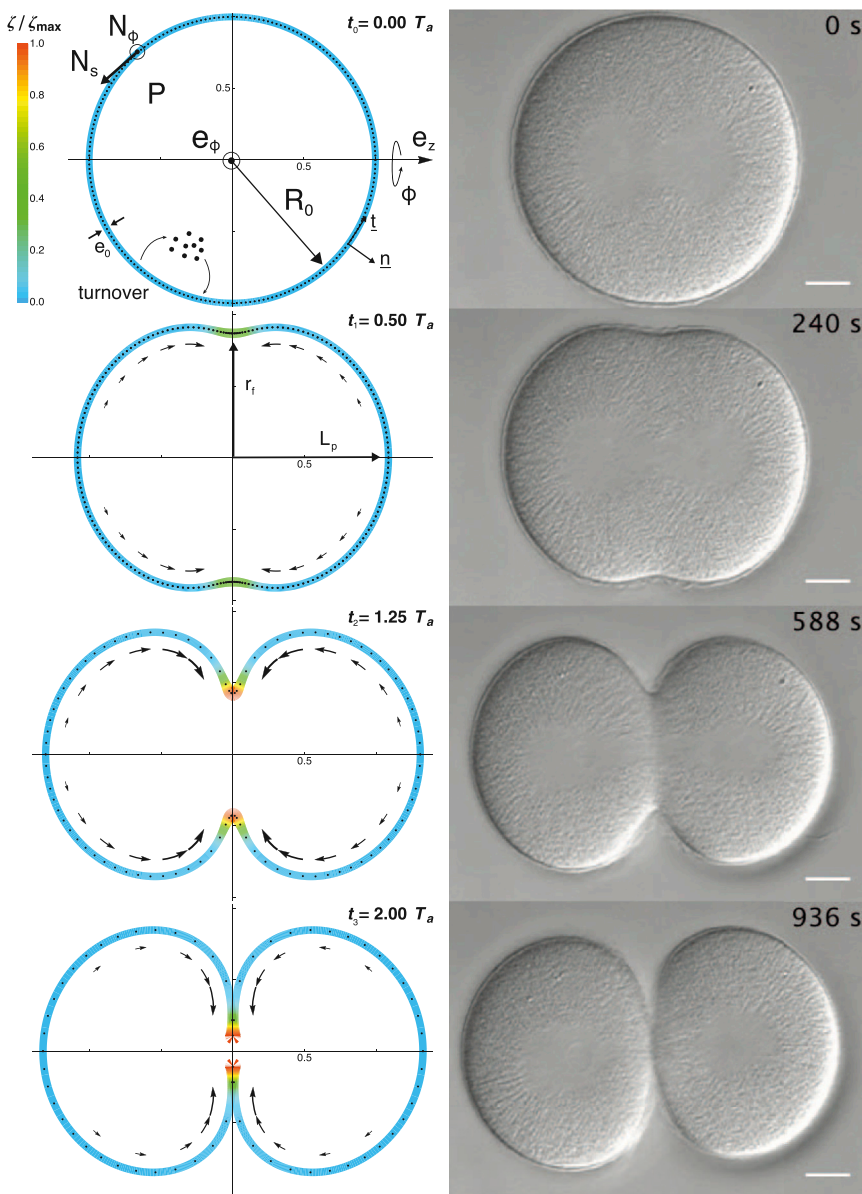


FIGURE 1 (Left) Numerical cell shape and cortex thickness evolution. (t_0) Initial spherical cortex of radius R_0 and main ingredients of the model. The membrane is axisymmetric around the axis \mathbf{e}_z and is subjected to internal tensions N_s and N_ϕ in its axial \mathbf{t} and azimuthal \mathbf{e}_ϕ principal directions, and to the cytoplasmic pressure P along its normal \mathbf{n} . The acto-myosin layer of initial thickness e_0 undergoes permanent turnover. Approximately 100 Lagrangian nodes are represented to follow the tangential membrane deformation over time (not all simulation nodes are shown). (t_1 , t_2 , and t_3) Cell cortex snapshots at successive times of constriction, in response to the rescaled myosin activity signal ζ/ζ_{\max} illustrated by the color shading. The value r_f is the furrow radius and L_p is the half pole-to-pole distance. Cortical flows along the membrane are represented by arrows of size proportional to the local tangent velocity. (Right) DIC microscopy images of a sand-dollar zygote (Dendroaster) deprived of its hyaline layer and jelly coat at four equivalent times of furrow constriction. The cell is not flattened and scale bar is 20 μm . (Credits: G. Von Dassow.) To see this figure in color, go online.

components, which are denoted by N_s and N_ϕ , respectively. The membrane tension is proportional to the cortical thickness e and is the sum of a viscous and an active contribution. Viscous tensions are proportional to the viscosity η , and to the axial and azimuthal strain rates, which are defined as the symmetric part of the membrane velocity gradient and denoted, respectively, by d_s and d_ϕ . Active tensions originate from molecular motors that steadily consume free energy coming from the hydrolysis of ATP molecules to produce work. The acto-myosin layer consists of a meshwork of semiflexible actin filaments suspended in the cytoplasmic fluid and myosin motors that bind to the filaments to exert contractile internal stresses. We use the active-gel theory of Kruse et al. (15,16) to describe the rheology of this material (see the [Supporting Material](#)). We neglect the polarity of actin filaments so that the active stress within the cortex results in an isotropic active membrane tension, proportional to the local activity $\zeta \geq 0$ of myosin motors and to the chemical free energy $\Delta\mu$ of hydrolysis of one ATP molecule. The membrane tensions finally read

$$N_s = \frac{e}{2} \zeta \Delta\mu + 2 \eta e (2 d_s + d_\phi), \quad (1a)$$

$$N_\phi = \frac{e}{2} \zeta \Delta\mu + 2 \eta e (d_s + 2 d_\phi), \quad (1b)$$

where ζ is proportional to the myosin phosphorylation, which is locally and temporally regulated by the active form of the protein RhoA (RhoA \cdot GTP) via its effector ROCK (23,41,42). Precise measurements of the spatio-temporal localization of RhoA \cdot GTP in several animal cells and embryos have shown an equatorial ring of active RhoA that positions the cleavage furrow (25,43): at onset of anaphase, active RhoA accumulates at the equator and forms along the acto-myosin cortex a Gaussian band of overactivity that causes cortical actin redistribution and furrowing. We mimic this active RhoA spatial zone by imposing along the membrane a Gaussian distribution of contractile overactivity $\delta\zeta^\infty$ centered at the equator,

$$\zeta(s, t) = \zeta_0 + \delta\zeta^\infty I(t) \exp\left(-\frac{1}{2} \left[\frac{s}{w}\right]^2\right), \quad (2)$$

where s is the curvilinear length from the equator along the membrane (see the [Supporting Material](#)); ζ_0 is the basal contractile activity in the membrane, responsible for cell poles' contractility; w is the signal width; $\delta\zeta^\infty$ is the amplitude of the overactivity; and $I(t)$ is a function of time varying from 0 to 1. The analysis of the RhoA \cdot GTP signal measurements performed in Bement et al. (25) shows that the signal amplitude increases rapidly at anaphase onset and saturates over the rest of furrow ingression. Although the precise form of the function $I(t)$ may depend on the organism and conditions, we choose for [Figs. 1 and 2](#) (and see [Movie S1](#) and [Movie S5](#)) a sigmoidal increase in time ([Fig. 2, inset](#)) that fits the experimental results reasonably well.

Polar actin filaments undergo permanent assembly and disassembly, preferentially polymerizing at their plus-end and depolymerizing at their minus-end. At the scale of the cortex there is therefore a permanent acto-myosin turnover, measured by FRAP. Actin polymerization nucleators are located near the plasma membrane, whereas the depolymerization acts in the bulk. We describe this material dynamics by a depolymerization rate k_d within the layer thickness and a polymerization velocity v_p from the plasma membrane surface. We consider an element of cortical layer of surface a and thickness e . Incompressibility of the gel and polymerization/depolymerization processes are captured by the following Lagrangian rate of cortical volume change:

$$\frac{d(ae)}{dt} = -k_d a e + v_p a. \quad (3)$$

The stationary thickness at zero surface deformation is given by the ratio of the polymerization velocity and depolymerization rate $e_0 \equiv v_p/k_d$, as proposed in Joanny et al. (44).

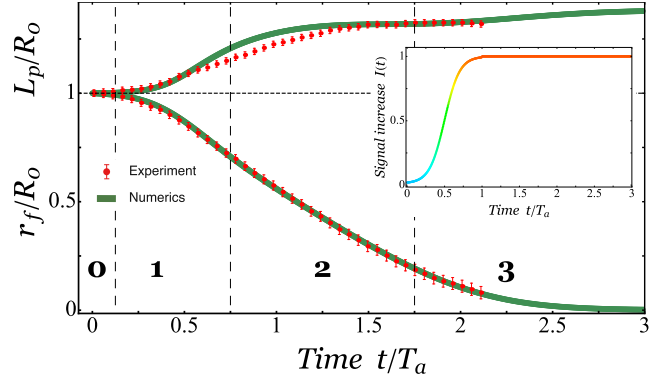


FIGURE 2 Furrow constriction dynamics. Time evolution of the furrow radius ($r_f = R_0$), and pole-to-pole half distance ($L_p = R_0$). Numerical results (line) are compared to experimental measurements of a sand-dollar zygote (points, data from the same DIC microscopy images of [Fig. 1](#)). (Vertical dashed lines) Delimiters of the four phases of constriction described in the text and numbered from 0 to 3. (Inset) Equatorial signal $I(t)$ applied as a function of time. To see this figure in color, go online.

Measurements show that the cytoplasmic volume is nearly conserved throughout cytokinesis (19,45). The cytoplasm is implemented here as a weakly compressible fluid with negligible viscosity. It applies therefore a uniform hydrostatic pressure onto the membrane,

$$P = -K(\mathcal{V} - \mathcal{V}_0), \quad (4)$$

where $\mathcal{V}_0 \equiv 4/3 \pi R_0^3$ is the initial cell volume. We use a value of the bulk modulus K large enough (see [Table S2](#) in the [Supporting Material](#)) to keep the volume change $|\mathcal{V} - \mathcal{V}_0|/\mathcal{V}_0$ below 0.1% in all our simulations (see [Fig. S4 A](#)). The force balance of the membrane tensions and the cytoplasmic pressure reads

$$\text{div}(N_s, N_\phi) + P \mathbf{n} = 0, \quad (5)$$

where the divergence operator depends nonlinearly on the actual configuration of the membrane. Its expression is provided in the [Supporting Material](#).

NUMERICAL RESULTS

The above equations are discretized in space by extending the method of Audoly et al. (46) to an axisymmetric geometry, as explained in the [Supporting Material](#). At every time step, the thickness and shape of the membrane are known; the unknown is the velocity field. The strain rates (d_s , d_ϕ) are expressed in terms of this velocity, and the tension is calculated by inserting the prescribed activity (Eq. 2) into Eq. 1. The balance of forces (Eq. 5) is solved for the velocity. By advecting the points of the membrane using this velocity field, we update its shape; the cortex thickness update follows from Eq. 3. To solve this set of dynamics equations (Eqs. 1–5), we adapted a preexisting C++ code (46) to the case of axisymmetric membranes. We analyzed and plotted numerical data using the software MATHEMATICA (Wolfram Alpha, <https://www.wolfram.com/mathematica/>).

In the initial state of the simulation, the membrane is a sphere with radius R_0 and uniform stationary thickness $e_0 = v_p/k_d$. It is subject to a uniform contractile activity ζ_0 . We note that the initial contractile stress ($\zeta_0 \Delta\mu/2$)

defines a typical active timescale when balanced with the viscous stress,

$$T_a \equiv \frac{2\eta}{\zeta_0 \Delta\mu}. \quad (6)$$

Typical numerical values for these parameters are picked from experimental references and summarized in Table S1.

Four phases of furrow constriction

An equatorial Gaussian band of overactivity $\delta\zeta^\infty = 75$ is progressively established according to the time profile $I(t)$ plotted in Fig. 2 (inset). The evolution of the shape and thickness of the cell cortex is shown in Fig. 1 (left) (see also Movie S1 and Movie S5): the four snapshots illustrate four distinct phases of constriction. The time evolution of the furrow radius r_f/R_0 and pole-to-pole distance L_p/R_0 (see definition in Fig. 1) are qualitatively different during each of the four phases, as shown in Fig. 2. Numerical results are compared in Fig. 1 to differential interference contrast (DIC) microscopy images of a sand-dollar zygote under cytokinesis and show very good agreement. Experimental time is rescaled by an active timescale T_a of value $468 \text{ s} \approx 8 \text{ min}$, to successfully match experimental furrow-radius and pole-to-pole distance evolutions with numerical results in Fig. 2. This timescale is perfectly consistent with the model approximations.

Phase 0: no overactivity

The initial spherical cell, shown at time $t_0 = 0$ in Fig. 1, is a stable equilibrium and verifies Laplace's law $P = e_0 \zeta_0 \Delta\mu / R_0$.

Phase 1: activity increase at the equator

Following the increase of myosin activity (inset in Fig. 2 and color shading in Fig. 1), the equatorial region becomes more contractile. It triggers a cortical flow toward the equator, as shown by the arrows at time $t_1 = 0.50 T_a$ in Fig. 1. This actin accumulation forms an annular bundle, thereby reproducing the observed formation of the contractile ring (47). This increase in thickness (see Fig. S2 B) results from the competition between cortical flow and actin turnover. The contractile ring starts to pinch the cell, increasing the cytoplasmic pressure (see Fig. S4 B); the pole-to-pole distance increases rapidly (Fig. 2, top) and the cell adopts a prolate-like shape (Fig. 1 and see Movie S1 and Movie S5 at time $t_1 = 0.50 T_a$), consistent with the so-called anaphase cell elongation (48).

Phase 2: plateau of activity at the equator

The amplitude of overactivity starts to saturate after a time interval of $\sim 0.75 T_a$ (Fig. 2, inset). The furrow adopts a constriction regime that is almost linear in time (Fig. 2, bottom). The pole's stretch is revealed by the increase in the gaps between the simulation nodes on snapshot $t_2 =$

$1.25 T_a$ in Fig. 1. The two future daughter cells become increasingly nonspherical, especially in the furrow region (see Movie S5). There, both the deformation and the tension are strongly anisotropic (see Fig. S3, C and D), leading to widely different radii of curvature in the axial and azimuthal directions.

Phase 3: slowing down of constriction

When the furrow radius approaches zero, the pole-to-pole distance reaches a relative plateau (Fig. 2, top). The constriction starts slowing down exponentially (Fig. 2, bottom), because viscous dissipation due to the constriction of the furrow increases as its radius decreases (see Fig. 7 D later in text, and see Fig. S5 B). A significant cortical flow persists from the poles toward the equator as long as the equatorial signal is maintained (time $t_3 = 2.00 T_a$ in Fig. 1). Because this flow is balanced by turnover, the shape and surface of the polar regions no longer evolve significantly with time (see Movie S1, Movie S4, and Fig. S4 C). If, on the contrary, the signal at the equator is significantly decreased after cytokinesis completion, the daughter cells adopt a spherical shape (see Movie S3). This behavior is classically observed in zygotes (deprived of the external shell) when cell-cell adhesion is artificially lowered.

A threshold for complete furrow constriction

We plot in Fig. 3 B the furrow ingression as a function of time for six values of the equatorial overactivity $\delta\zeta^\infty/\zeta_0$ between 10 and 100. For $\delta\zeta^\infty/\zeta_0 > 40$, the furrow fully constricts (see *silhouetted numbers* 4–6), but slows down when the equatorial signal is decreased. For $\delta\zeta^\infty/\zeta_0 \leq 40$, the furrow radius reaches a plateau (see *silhouetted numbers* 1–3). Full constriction therefore requires that the overactivity at the equator exceeds a threshold, and the rate of constriction is dose-dependent, consistent with observations reported in Loria et al. (49). The final stationary furrow radius r_f^∞ is plotted as a function of the overactivity amplitude $\delta\zeta^\infty/\zeta_0$ in Fig. 3 A. The diagram displays a saddle-node bifurcation near $\delta\zeta^\infty/\zeta_0 \approx 40$. The longer delay required to complete ingression around the threshold (Fig. 3 B, *silhouetted number* 4) is therefore interpreted as a critical slowing-down. Shape evolutions leading to constriction failure and completion are compared in Movie S2 (left, *silhouetted number* 2; right, *silhouetted number* 5).

The bifurcation diagram in Fig. 3 A reveals furthermore a noticeable hysteretic behavior, represented by the arrows. If one starts from a fully constricted state at the end of cytokinesis ($r_f \approx 0$ and $\delta\zeta^\infty/\zeta_0 > 40$) and decreases the equatorial overactivity under the threshold $\delta\zeta^\infty/\zeta_0 < 40$, the cell stays divided (unless the signal is decreased down to zero). As long as some slight equatorial tension is maintained, the divided state is therefore mechanically stable, which may prevent the furrow from regressing erroneously during the

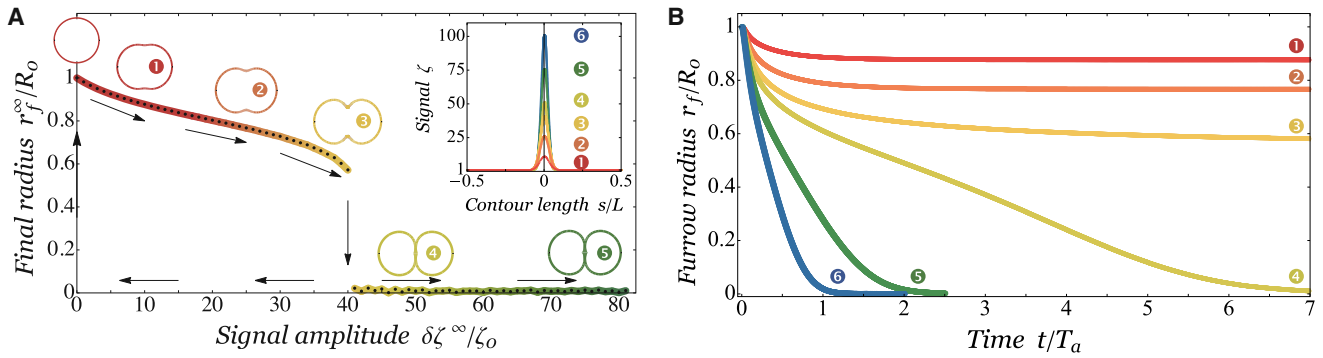


FIGURE 3 Constriction completion and failure. (A) Bifurcation diagram representing the final furrow radius r_f^∞/R_0 as a function of the amplitude of equatorial overactivity $\delta\zeta^\infty/\zeta_0$. The diagram displays a jump from constriction failure to completion for a critical amplitude $\delta\zeta^\infty/\zeta_0 \approx 40$. Final cell shapes are plotted for the six activity signals ζ , of amplitudes $\delta\zeta^\infty/\zeta_0 = 10$ (1), 25 (2), 40 (3), 50 (4), 75 (5), and 100 (6) as represented (inset) as a function of the contour length from equator s/L along the membrane (of length L). (Arrows) Hysteresis loop. Starting from a divided state above the threshold (6, for example), we decrease the equatorial signal: the cell remains divided, unless the signal is dropped down to 0—the point at which it goes back to the spherical state. (B) Furrow radius evolution r_f/R_0 as a function of time t/T_a for the six signals ζ (represented in panel A, inset). To see this figure in color, go online.

midbody formation (50). However, if the signal is decreased prematurely in the course of ingression (for $r_f/R_0 > 0.6$), the furrow regresses and cytokinesis fails, as presumably happens in Argiros et al. (51). A tight synchronization between the signaling machinery and the furrow constriction is therefore essential. The two scenarios are compared in Movie S3 with experiments.

Constriction dynamics depends on turnover

In Fig. 4 and Movie S4 we compare the constriction dynamics for three different turnover rates $k_d T_a = 30$ (circled 1), $k_d T_a = 40$ (circled 2), and $k_d T_a = 80$ (circled 3) while keeping $e_0 = v_p/k_d$ and $\delta\zeta^\infty/\zeta_0 = 75$ constant. The stationary thickness e_f^∞ in the furrow results from a competition between incoming cortical flows and turnover, and therefore decreases at higher turnover rates (Fig. 4, inset). The active tension in the furrow is proportional to the local thickness (Eq. 1) and therefore decreases at high turnover rates, which

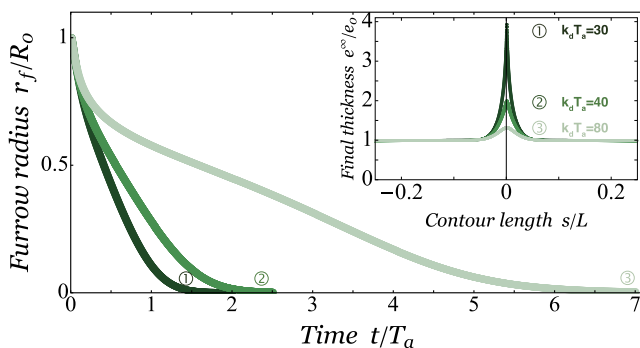


FIGURE 4 Influence of turnover on constriction. Furrow radius $r_f = R_0$ as a function of normalized time $t = T_a$ for three turnover rates: $k_d T_a = 30$ (1), $k_d T_a = 40$ (2), and $k_d T_a = 80$ (3). (Inset) Corresponding steady-state membrane thickness $e_1 = e_0$ along the rescaled contour length $s = L$ from equator (L is the total membrane midline length). To see this figure in color, go online.

lowers the rate of furrow ingression as shown on Fig. 4. We expect a large increase of turnover to impair the completion of the furrow ingression if the equatorial signal is close to the constriction threshold. Actin turnover is therefore a critical variable for cytokinesis completion; it has to be tightly regulated by the cell directly via depolymerization and polymerization and indirectly via active cortical flows.

Cytokinesis duration is independent of initial cell size

The duration of cytokinesis has been recently reported to be independent of cell initial size in *Caenorhabditis elegans* embryos (52). This remarkable property ensures the tight synchronization of daughter cells development during embryogenesis. We performed numerical constrictions with various initial cell size radii R_0 between 0.5 and 4. Measurements performed on embryos of several organisms (25) revealed the existence of a linear relationship between the initial cell size R_0 and the width w of the Gaussian RhoA-GTP zone: we thus choose w proportionally to R_0 , keeping all the other parameters constant (see Table S1). The evolution of the furrow radius with time is plotted in Fig. 5 for four different values of R_0 and w . We observe that the duration of furrow constriction is independent of R_0 provided that $w \propto R_0$. Our model reproduces this robust feature of cytokinesis.

SCALING MODEL

The numerical results can be interpreted in terms of scaling arguments based on a minimal geometry sketched in Fig. 6 A, that was proposed in 1972 by Yoneda and Dan (53). The cell poles are represented by two portions of sphere of radius R under constant active tension $N^a_0 = e_0 \zeta_0 \Delta\mu/2$ and are connected by a ring of radius r_f and width w . The contractile ring is submitted to an active line

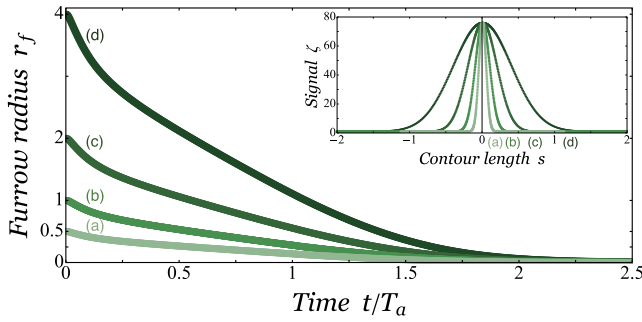


FIGURE 5 Cytokinesis duration is independent of initial cell size. Furrow radius r_f as a function of time $t = T_a$ for four initial cell radii $R_0 = 0.5, 1, 2$, and 4 . (Inset) Corresponding Gaussian activity signals of width w proportional to R_0 , plotted as a function of the membrane midline contour length s . To see this figure in color, go online.

tension $\gamma \approx w(N_f^a - N_0^a)$, where N_f^a is the mean contractile surface tension in the furrow. The competition with cortical tension at cell poles is measured by the dimensionless parameter

$$\kappa = \frac{\gamma}{2R_0 N_0^a} \approx \frac{w}{2R_0} \left(N_f^a - N_0^a \right) / N_0^a.$$

The opening angle θ defined in Fig. 6 A is a measure of the constriction state of the cell.

Cytokinesis completion is controlled by the difference of contractility between the contractile ring and the poles

The polar contractility tends to reduce the surface $A_p = 4\pi R^2(1 + \cos\theta)$ of the cell poles, whereas the line tension tends to reduce the contractile ring circumference $r_f = R \sin \theta$. These effects are captured by a simple mechanical energy $\varepsilon = 2\pi r_f \gamma + 2A_p N_0^a$. Cytoplasmic volume conservation can be written as $R_0 = R F(\theta)^{1/3}$, where $F(\theta)$ is a smooth function of θ defined in the Supporting Material. The mechanical energy, rescaled by $\varepsilon_0 = 4\pi R_0^2 N_0^a$ for a spherical cell, depends only on κ and θ and reads

$$\frac{\varepsilon}{\varepsilon_0} = \frac{\kappa \sin \theta}{F(\theta)^{1/3}} + \frac{1 + \cos \theta}{F(\theta)^{2/3}}. \quad (7)$$

We plotted in Fig. 6 B the mechanical energy $\varepsilon/\varepsilon_0$ as a function of θ for various values of κ . The minima of $\varepsilon/\varepsilon_0$ are the local equilibrium states of the cell. Starting from a spherical cell at $\theta = \pi/2$, the final shape is reached at the first local minimum of energy. For $\kappa = 0$ (red curve), in absence of any contractile ring, the spherical cell $\theta = \pi/2$ is the minimum of energy. As the control parameter κ increases, i.e., the contractile ring line tension increases, the first local minimum of ε shifts toward a more constricted state ($\theta = \pi/2$), but the constriction is still incomplete. For $\kappa \geq 0.4$, the local minimum disappears at the benefit of a single global minimum, corresponding to the fully constricted state $\theta = 0$

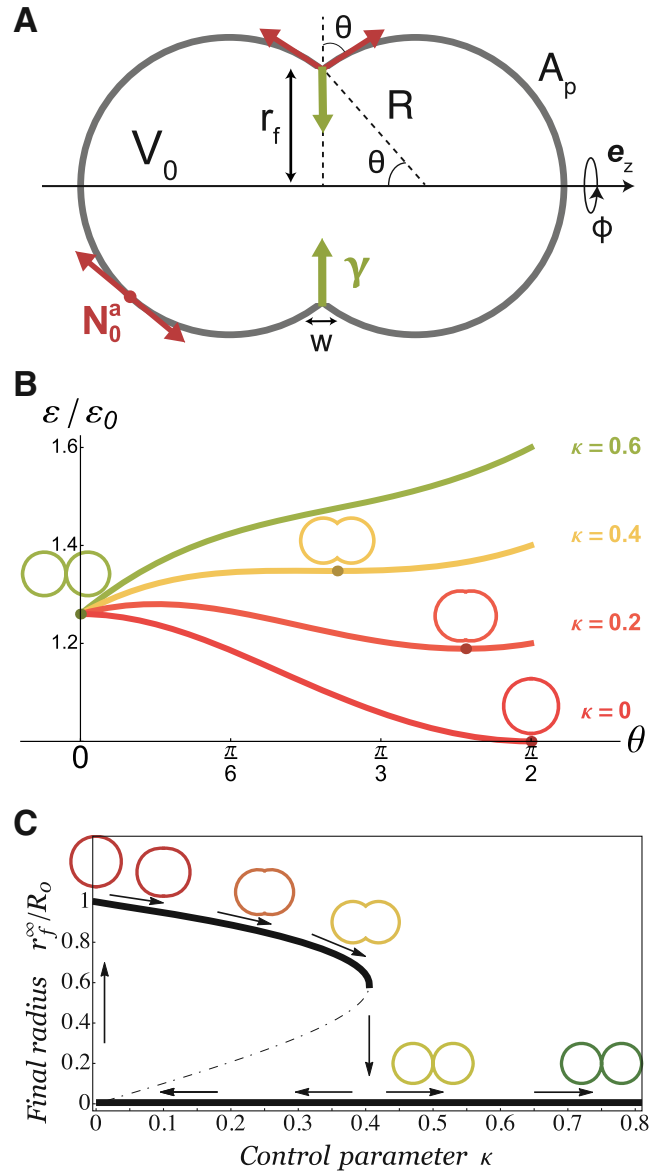


FIGURE 6 Scaling model. (A) Sketch of the minimal geometry proposed by Yoneda and Dan (53): Two portions of sphere of surface A_p and surface tension N_0^a are pinched by an equatorial ring of radius r_f , of width w , and of line tension γ . The opening angle θ characterizes the constriction state of the cell and the cytoplasmic volume-enclosed V_0 is conserved. (B) Mechanical energy profile $E = E_0$ as a function of the constriction state θ for four values of $\kappa = \gamma/2R_0 N_0^a$. Local minima of the energy correspond to equilibrium states (darker points), above which are plotted the corresponding cell shapes. (C) Bifurcation diagram representing the final furrow radius r_f^∞/R_0 as a function of the control parameter κ . The upper branch and the branch $r_f = 0$ are stable branches, but one branch (dot-dashed) is unstable. The critical point is a saddle-node, and the bifurcation classically exhibits an hysteresis (see arrows). Final cell shapes, starting from a spherical cell, are plotted for the six following values of the control parameter: $\kappa = 0, 0.1, 0.25, 0.4, 0.5$, and 0.75 . To see this figure in color, go online.

(green curve): constriction succeeds. This simple energetic approach of the constriction completion uncovers the fundamental mechanism of cytokinesis: cell-volume conservation enforces a competition between the line tension of the ring

(which tends to minimize its circumference) and the contractility of the poles (which resists the associated cell-surface increase).

This competition drives a first-order transition from cytokinesis failure to constriction completion. We plot alternately in Fig. 6 C the bifurcation diagram of the final constriction state r_f^∞ (corresponding to the first minimum of energy in Fig. 6 B) as a function of the control parameter κ . Similarly to the numerical results (Fig. 3 A), scaling arguments reveal a jump from partial to complete constriction above a critical threshold of the difference of contractility between the furrow and the poles, of value $\kappa \approx 0.4$ (see the Supporting Material). The energy plot in Fig. 6 B shows clearly that $\theta = 0$ is a possible local energy minimum for $\kappa > 0$, and therefore that the divided state is mechanically stable, which clarifies the origin of the hysteresis behavior, illustrated by arrows on Fig. 6 C.

The contractility difference between the contractile ring and poles also controls the dynamics of constriction

The mechanical power of active effects (Eq. 7) is exactly dissipated by viscous cell deformations (see numerical results in Fig. S5 A). The viscous dissipation is made of two contributions, the stretching of the poles and the constriction of the ring, which we estimate in scaling. The volume of acto-myosin in the poles is $V_p = 2A_p e_p$ and in the ring $V_f = 2\pi r_f w e_f$, where w and e_f are the width and thickness of the contractile ring. According to the numerical results (see Fig. S2 D), the thickness of the actin layer at poles does not vary appreciably. The value $e_p \approx e_0$ and the ring thickness e_f reach a steady-state value that depends on turnover. This yields the viscous dissipated power

$$\mathcal{P}_d = \frac{1}{2} \eta \left[V_p \left(\frac{1}{R} \frac{dr_f}{dt} \right)^2 + V_f \left(\frac{1}{r_f} \frac{dr_f}{dt} \right)^2 \right]. \quad (8)$$

From the balance of mechanical and dissipated powers $d\mathcal{E}/dt + \mathcal{P}_d = 0$, we calculate the rate of furrow constriction as a positive function \mathcal{H} of θ , κ , and λ only (see the Supporting Material)

$$T_a \frac{dr_f}{dt} = -R_0 \mathcal{H}(\theta, \kappa, \lambda), \quad \text{with } \lambda \equiv \frac{e_f}{e_0} \frac{w}{2R_0}. \quad (9)$$

From Eq. 9, we can solve for the furrow radius r_f as a function of time and conclude that

1. The constriction timescale is set by $T_a = \eta e_0 / N^a_0$, as defined in Eq. 6, which measures the typical active time of viscous stretching of the poles.
2. The values κ and λ control the rate of constriction, and

$$\kappa \approx \frac{w}{2R_0} \left(\frac{\zeta_f e_f}{\zeta_0 e_0} - 1 \right)$$

characterizes the dependence of the constriction rate on the contractility difference between the ring and the poles, and depends on the normalized furrow activity ζ_f/ζ_0 and on turnover via the normalized thickness e_f/e_0 . The value λ depends essentially on turnover via e_f . We plot in Fig. 7 A the furrow radius r_f evolution as a function of time for various values of κ between 0.1 and 1, at fixed $\lambda = 0.1$, and recover qualitatively the same dynamics as in the numerical results. In Fig. 7 B we keep ζ_f/ζ_0 constant and plot r_f as a function of time t/T_a for four values of e_f/e_0 between 1 and 4, thereby mimicking the competition between cortical flows and actin turnover. Again we retrieve qualitatively the same behavior as for the continuous model: decreasing the furrow thickness e_f , thereby enhancing turnover, slows down the constriction and can even impede its completion (see curve $e_f/e_0 = 1$).

3. If we assume that w scales linearly with R_0 , then we find that κ and λ , which are both proportional to w/R_0 , become independent of the initial cell radius and so does \mathcal{H} . The constriction rate in Eq. 9 is proportional to the initial radius, and the cytokinesis duration becomes independent of initial cell size, as illustrated on Fig. 7 C, which reproduces the numerical results of Fig. 5.

We show that the dissipation associated to the poles stretching participates largely to the slowing-down of furrow constriction, consistently with numerical results (see Fig. S5 B): the decrease of r_f is indeed much more rapid in Fig. 7 D for vanishing poles dissipation ($V_p \rightarrow 0$ in Eq. 8). These results suggest that the contractility and the viscosity of the polar cortex are both critical parameters to consider in accounting for the dynamics of furrow constriction. In the limiting case of an isolated visco-active ring (no poles at all), scaling arguments yield a purely exponential constriction dynamics (dashed line in Fig. 7 D), consistent with experimental contraction of isolated rings in vitro (54). We can retrieve this scaling by a simple balance of viscous forces $\eta w e_f / r_f dr_f/dt$ with the constricting force $\gamma = w N^a_f = w e_f \zeta_f \Delta\mu$ in the ring, which leads immediately to $r_f/R_0 = e^{-\tau t}$, with $\tau = 2\eta/\zeta_f \Delta\mu$ the characteristic active timescale of the problem. The constriction dynamics of an isolated visco-active ring depends, therefore, strongly on the ratio of myosin activity ζ_f and acto-myosin viscosity η (controlled by cross-linking) but becomes independent of actin turnover, consistent with recent experimental results (55).

DISCUSSION

Using both numerical and scaling analyses, we rationalize the physical mechanisms governing ring constriction in the cytokinesis of animal cells. Following the seminal work of White and Borisy (6) and Bray and White (56), we show that a gradient of surface contractility from the poles to the

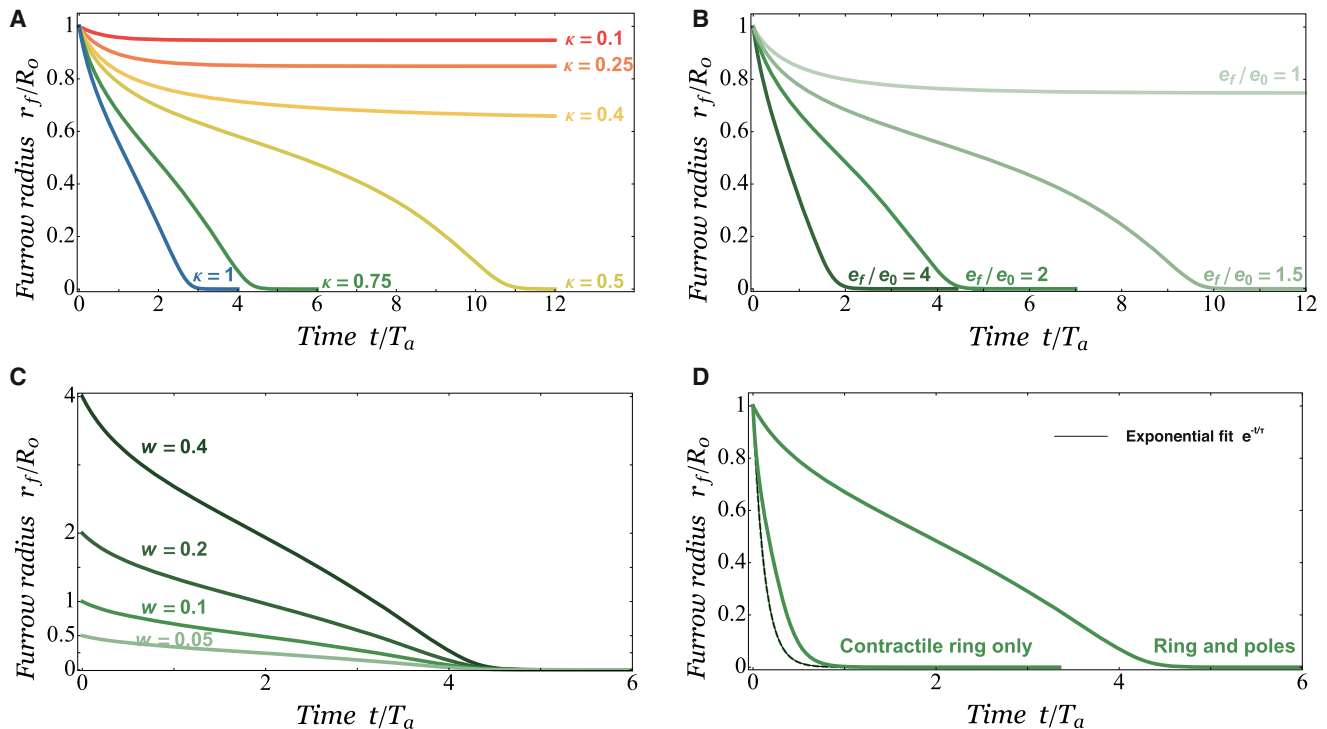


FIGURE 7 Constriction dynamics in scaling. Normalized furrow radius evolution r_f/R_0 with time t/T_a . (A) For $\kappa = 0.1, 0.25, 0.4, 0.5, 0.75$, and 1 , with constant $\lambda = 0.1$. For $\kappa \leq 0.4$, the furrow radius reaches a plateau indicating constriction failure, whereas for $\kappa \geq 0.4$ constriction is complete and its speed increases with κ . (B) For $e_f = e_0$ between 1 and 4 , keeping $\zeta_f/\zeta_0 = 8$ and $w = R_0 = 0.1$ constant. Constriction slows down when $e_f = e_0$ decreases from 4 to 1.5 , and can even fail when it drops to 1 . (C) For four initial cell radii $R_0 = 0.5, 1, 2$, and 4 , where the ring width w is increased proportionally, $w = 0.05, 0.1, 0.2$, and 0.4 . The values $e_f = e_0 = 2$ and $\zeta_f/\zeta_0 = 8$ are maintained constant. The rate of constriction increases proportionally to the ring width, leading to the same constriction duration for the four cell sizes. (D) For a cell with dissipation due to the ring constriction only and with dissipation due to poles stretching and ring constriction ($\zeta_f/\zeta_0 = 8$, $e_f = e_0 = 2$, $w = R_0 = 0.1$). (Dashed line) Constriction of an isolated ring (no poles) fitted with the exponential function $e^{-t/\tau}$ with $\tau = 2\eta/\zeta_f \Delta\mu$. To see this figure in color, go online.

equator is sufficient to drive cytokinesis and to reproduce its main features: formation of the contractile ring, cortical flow toward the equator, and furrow constriction. Starting from a quite fundamental physical model of the cortex—a thin viscous layer producing active contraction and subjected to a uniform cytoplasmic pressure—we are able to reproduce realistic shapes of dividing embryos. We provide quantitative criteria for cytokinesis completion and propose a general framework for interpreting and characterizing constriction failure. We furthermore demonstrate the physical mechanism leading to the independence of cytokinesis duration on the initial cell size in embryos (52), and we highlight the critical influence of actin turnover.

A scaling model is then proposed to interpret the numerical results. It explains and successfully reproduces the properties of furrow constriction, despite its simplified geometry. It notably demonstrates that the contractility difference between the poles and the furrow is the key parameter for both cytokinesis completion and constriction dynamics. This highlights a critical role of the polar cortex in cytokinesis success and dynamics.

We reproduce accurately the experimental constriction dynamics and shape evolution of a sand-dollar embryo. Pre-

cise spatio-temporal measurements of RhoA-GTP along the cortex over the entire time of constriction would, however, be required for our simulation to reproduce an experiment in full detail. Estimates of cortex turnover are also required to account for the accumulation of actin in the ring via cortical flows, which can play a major role in constriction dynamics. FRAP measurements of the cortex provide reasonable values for the turnover timescale (36), but we have neglected here the possible nonuniformity of turnover along the cortex for the sake of simplicity. RhoA-GTP is indeed known for also promoting actin polymerization via the formin mDia1 (23), and the ring formation is, then, likely to be the result of accumulation by cortical flows and higher polymerization (34,35). In contrast to this, myosin activity, promoted by RhoA-GTP via its effector ROCK, has been shown to enhance actin filament disassembly both in vitro and in vivo (34,57). Altogether, the local activation of RhoA is likely to enhance nonuniform turnover. A more rigorous implementation of nonuniform turnover would require substantial progress in the theoretical understanding and quantitative characterization of in vivo disassembly of actin by myosin motors, which is far beyond this study. We argue nevertheless that the

fundamental trends highlighted in our study will remain valid. Based on quantitative studies in *C. elegans* (58), our model assumed that the frictional loss associated with cortex sliding along the plasma membrane and cytosol was negligible compared to viscous dissipation associated with cortex deformation. It would, however, be interesting to evaluate the effect of friction on the constriction dynamics in a further development of the model.

Our model demonstrates that the equatorial contractile region does not need to be structurally different from the rest of the cortex, but only more contractile. The actin filament orientation may, however, be anisotropic in the membrane plane, in particular in the furrow region (59), because their spatial organization is expected to be dynamically coupled to cortical flows (15,16). We expect that our results will not be changed qualitatively if the flow alignment effects are taken into account, but we can conjecture that the alignment of actin filaments in the furrow (7,38) lowers the activity threshold for full constriction.

Finally, we would expect the threshold value to drop rapidly, or even to vanish, if the constraint of cytoplasm incompressibility is partially relaxed (as would happen, for instance, by the release of cytoplasmic fluid through membrane pores). Conversely, constriction success may be impaired by a significant increase of cytoplasmic bulk viscoelasticity (60). Variability among animal species and among differentiated cells in an otherwise same organism may thus be revealed by different strategies for ensuring constriction success. These subtle physical effects suggest future lines for experimental investigations and potential improvements of our description and understanding of furrow constriction in animal cell cytokinesis.

SUPPORTING MATERIAL

Continuous Model, Discrete Formulation, Numerical Implementation, Scaling Model, two tables, six figures, 58 equations, five movies and references (61–70) are available at [http://www.biophysj.org/biophysj/supplemental/S0006-3495\(13\)01244-7](http://www.biophysj.org/biophysj/supplemental/S0006-3495(13)01244-7).

The authors are very grateful to G. Von Dassow and C. B. Shuster for providing experimental videos of dividing embryos and thank M. Piel and C. Roubinet for helpful comments on the manuscript.

This work was supported by the European network MitoSys project.

REFERENCES

1. Eggert, U. S., T. J. Mitchison, and C. M. Field. 2006. Animal cytokinesis: from parts list to mechanisms. *Annu. Rev. Biochem.* 75:543–566.
2. Fujiwara, T., M. Bandi, ..., D. Pellman. 2005. Cytokinesis failure generating tetraploids promotes tumorigenesis in p53-null cells. *Nature*. 437:1043–1047.
3. Green, R. A., E. Paluch, and K. Oegema. 2012. Cytokinesis in animal cells. *Annu. Rev. Cell Dev. Biol.* 28:29–58.
4. Greenspan, H. P. 1978. On fluid-mechanical simulations of cell division and movement. *J. Theor. Biol.* 70:125–134.
5. Akkas, N. 1980. On the biomechanics of cytokinesis in animal cells. *J. Biomech.* 13:977–988.
6. White, J. G., and G. G. Borisy. 1983. On the mechanisms of cytokinesis in animal cells. *J. Theor. Biol.* 101:289–316.
7. Zinemanas, D., and A. Nir. 1987. On the viscous deformation of biological cells under anisotropic surface tension. *J. Fluid Mech.* 193:217–241.
8. He, X., and M. Dembo. 1997. On the mechanics of the first cleavage division of the sea urchin egg. *Exp. Cell Res.* 233:252–273.
9. Hiramato, Y. 1971. A photographic analysis of protoplasmic movement during cleavage in the sea urchin egg. *Dev. Growth Differ.* 13:191–200.
10. Zhang, W., and D. N. Robinson. 2005. Balance of actively generated contractile and resistive forces controls cytokinesis dynamics. *Proc. Natl. Acad. Sci. USA*. 102:7186–7191.
11. Zumdick, A., M. Cosentino Lagomarsino, ..., F. Jülicher. 2005. Continuum description of the cytoskeleton: ring formation in the cell cortex. *Phys. Rev. Lett.* 95:258103.
12. Srivastava, P., R. Shlomovitz, ..., M. Rao. 2013. Patterning of polar active filaments on a tense cylindrical membrane. *Phys. Rev. Lett.* 110:168104.
13. Zumdick, A., K. Kruse, ..., F. Jülicher. 2007. Stress generation and filament turnover during actin ring constriction. *PLoS ONE*. 2:e696.
14. Mendes Pinto, I., B. Rubinstein, ..., R. Li. 2012. Actin depolymerization drives actomyosin ring contraction during budding yeast cytokinesis. *Dev. Cell*. 22:1247–1260.
15. Kruse, K., J.-F. Joanny, ..., K. Sekimoto. 2005. Generic theory of active polar gels: a paradigm for cytoskeletal dynamics. *Eur. Phys. J. E Soft Matter*. 16:5–16.
16. Marchetti, M. C., J.-F. Joanny, ..., R. A. Simha. 2013. Hydrodynamics of soft active matter. *Rev. Mod. Phys.* 85:1143.
17. Poirier, C. C., W. P. Ng, ..., P. A. Iglesias. 2012. Deconvolution of the cellular force-generating subsystems that govern cytokinesis furrow ingression. *PLOS Comput. Biol.* 8:e1002467.
18. Rankin, K. E., and L. Wordeman. 2010. Long astral microtubules uncouple mitotic spindles from the cytokinetic furrow. *J. Cell Biol.* 190:35–43.
19. Sedzinski, J., M. Biro, ..., E. Paluch. 2011. Polar actomyosin contractility destabilizes the position of the cytokinetic furrow. *Nature*. 476:462–466.
20. Fletcher, D. A., and R. D. Mullins. 2010. Cell mechanics and the cytoskeleton. *Nature*. 463:485–492.
21. Mabuchi, I., and M. Okuno. 1977. The effect of myosin antibody on the division of starfish blastomeres. *J. Cell Biol.* 74:251–263.
22. Straight, A. F., A. Cheung, ..., T. J. Mitchison. 2003. Dissecting temporal and spatial control of cytokinesis with a myosin II inhibitor. *Science*. 299:1743–1747.
23. Dean, S. O., S. L. Rogers, ..., J. A. Spudis. 2005. Distinct pathways control recruitment and maintenance of myosin II at the cleavage furrow during cytokinesis. *Proc. Natl. Acad. Sci. USA*. 102:13473–13478.
24. von Dassow, G., K. J. C. Verbrugghe, ..., W. M. Bement. 2009. Action at a distance during cytokinesis. *J. Cell Biol.* 187:831–845.
25. Bement, W. M., H. A. Benink, and G. von Dassow. 2005. A microtubule-dependent zone of active RhoA during cleavage plane specification. *J. Cell Biol.* 170:91–101.
26. Su, K.-C., T. Takaki, and M. Petronczki. 2011. Targeting of the RhoGEF Ect2 to the equatorial membrane controls cleavage furrow formation during cytokinesis. *Dev. Cell*. 21:1104–1115.
27. Atilgan, E., D. Burgess, and F. Chang. 2012. Localization of cytokinesis factors to the future cell division site by microtubule-dependent transport. *Cytoskeleton (Hoboken)*. 69:973–982.
28. Rappaport, R. 1996. Cytokinesis in Animal Cells. Cambridge University Press, Cambridge, UK.
29. Tinevez, J. Y., U. Schulze, ..., E. Paluch. 2009. Role of cortical tension in bleb growth. *Proc. Natl. Acad. Sci. USA*. 106:18581–18586.

30. Sinha, B., D. Köster, ..., P. Nassoy. 2011. Cells respond to mechanical stress by rapid disassembly of caveolae. *Cell*. 144:402–413.
31. Albertson, R., B. Riggs, and W. Sullivan. 2005. Membrane traffic: a driving force in cytokinesis. *Trends Cell Biol.* 15:92–101.
32. Dyer, N., E. Rebollo, ..., M. González-Gaitán. 2007. Spermatocyte cytokinesis requires rapid membrane addition mediated by ARF6 on central spindle recycling endosomes. *Development*. 134:4437–4447.
33. Charras, G. T., J. C. Yarrow, ..., T. J. Mitchison. 2005. Non-equilibration of hydrostatic pressure in blebbing cells. *Nature*. 435:365–369.
34. Guha, M., M. Zhou, and Y. L. Wang. 2005. Cortical actin turnover during cytokinesis requires myosin II. *Curr. Biol.* 15:732–736.
35. Murthy, K., and P. Wadsworth. 2005. Myosin-II-dependent localization and dynamics of F-actin during cytokinesis. *Curr. Biol.* 15:724–731.
36. Fritzsche, M., A. Lewalle, ..., G. T. Charras. 2013. Analysis of turnover dynamics of the submembranous actin cortex. *Mol. Biol. Cell*. 24:757–767.
37. Batchelor, G. K. 1967. An Introduction to Fluid Dynamics. Cambridge University Press, Cambridge, UK.
38. Salbreux, G., J. Prost, and J.-F. Joanny. 2009. Hydrodynamics of cellular cortical flows and the formation of contractile rings. *Phys. Rev. Lett.* 103:058102.
39. Green, A. E., and W. Zerna. 2002. Theoretical Elasticity. Dover Publications, Mineola, NY, pp. 386–389.
40. Maddox, A. S., and K. Burridge. 2003. RhoA is required for cortical retraction and rigidity during mitotic cell rounding. *J. Cell Biol.* 160:255–265.
41. Kimura, K., M. Ito, ..., K. Kaibuchi. 1996. Regulation of myosin phosphatase by Rho and Rho-associated kinase (Rho-kinase). *Science*. 273:245–248.
42. Uehara, R., G. Goshima, ..., E. R. Griffiths. 2010. Determinants of myosin II cortical localization during cytokinesis. *Curr. Biol.* 20:1080–1085.
43. Yoshizaki, H., Y. Ohba, ..., M. Matsuda. 2003. Activity of Rho-family GTPases during cell division as visualized with FRET-based probes. *J. Cell Biol.* 162:223–232.
44. Joanny, J. F., K. Kruse, ..., S. Ramaswamy. 2013. The actin cortex as an active wetting layer. *Eur. Phys. J. E Soft Matter*. 36:52–58.
45. Hiramoto, Y. 1958. A quantitative analysis of protoplasmic movement during cleavage in the sea urchin egg. *J. Exp. Biol.* 35:407–424.
46. Audoly, B., N. Clauvelin, ..., M. Wardetzky. 2013. A discrete geometric approach for simulating the dynamics of thin viscous threads. *J. Comput. Phys.* 253:18–49.
47. Cao, L. G., and Y. L. Wang. 1990. Mechanism of the formation of contractile ring in dividing cultured animal cells. II. Cortical movement of microinjected actin filaments. *J. Cell Biol.* 111:1905–1911.
48. Hickson, G. R. X., A. Echard, and P. H. O'Farrell. 2006. Rho-kinase controls cell shape changes during cytokinesis. *Curr. Biol.* 16:359–370.
49. Loria, A., K. M. Longhini, and M. Glotzer. 2012. The RhoGAP domain of CYK-4 has an essential role in RhoA activation. *Curr. Biol.* 22:213–219.
50. Lekomtsev, S., K.-C. Su, ..., M. Petronczki. 2012. Centralspindlin links the mitotic spindle to the plasma membrane during cytokinesis. *Nature*. 492:276–279.
51. Argiros, H., L. Henson, ..., C. B. Shuster. 2012. Centralspindlin and chromosomal passenger complex behavior during normal and Rappaport furrow specification in echinoderm embryos. *Cytoskeleton (Hoboken)*. 69:840–853.
52. Carvalho, A., A. Desai, and K. Oegema. 2009. Structural memory in the contractile ring makes the duration of cytokinesis independent of cell size. *Cell*. 137:926–937.
53. Yoneda, M., and K. Dan. 1972. Tension at the surface of the dividing sea-urchin egg. *J. Exp. Biol.* 57:575–587.
54. Reymann, A.-C., R. Boujemaa-Paterski, ..., L. Blanchoin. 2012. Actin network architecture can determine myosin motor activity. *Science*. 336:1310–1314.
55. Mishra, M., J. Kashiwazaki, ..., I. Mabuchi. 2013. In vitro contraction of cytokinetic ring depends on myosin II but not on actin dynamics. *Nat. Cell Biol.* 15:853–859.
56. Bray, D., and J. G. White. 1988. Cortical flow in animal cells. *Science*. 239:883–888.
57. Murrell, M. P., and M. L. Gardel. 2012. F-actin buckling coordinates contractility and severing in a biomimetic acto-myosin cortex. *Proc. Natl. Acad. Sci. USA*. 109:20820–20825.
58. Mayer, M., M. Depken, ..., S. W. Grill. 2010. Anisotropies in cortical tension reveal the physical basis of polarizing cortical flows. *Nature*. 467:617–621.
59. Fishkind, D. J., and Y. L. Wang. 1993. Orientation and three-dimensional organization of actin filaments in dividing cultured cells. *J. Cell Biol.* 123:837–848.
60. Moulding, D. A., E. Moeendarbary, ..., A. J. Thrasher. 2012. Excess F-actin mechanically impedes mitosis leading to cytokinesis failure in X-linked neutropenia by exceeding Aurora B kinase error correction capacity. *Blood*. 120:3803–3811.
61. Yeung, A., and E. Evans. 1989. Cortical shell-liquid core model for passive flow of liquid-like spherical cells into micropipets. *Biophys. J.* 56:139–149.
62. Daniels, B. R., B. C. Masi, and D. Wirtz. 2006. Probing single-cell micromechanics in vivo: the microrheology of *C. elegans* developing embryos. *Biophys. J.* 90:4712–4719.
63. Charras, G. T., T. J. Mitchison, and L. Mahadevan. 2009. Animal cell hydraulics. *J. Cell Sci.* 122:3233–3241.
64. Kalwarczyk, T., N. Ziebac, ..., R. Holyst. 2011. Comparative analysis of viscosity of complex liquids and cytoplasm of mammalian cells at the nanoscale. *Nano Lett.* 11:2157–2163.
65. Spek, J. 1918. Surface tension differences as a cause of cell division [Oberflächenspannungsdifferenzen als eine Ursache der Zellteilung]. *Arch. Entwicklungsmech. Org.* 44:5–113.
66. Dan, K., T. Yanagita, and M. Sugiyama. 1937. Behavior of the cell surface during cleavage. I. *Protoplasma*. 28:66–81.
67. Happel, J., and H. Brenner. 1983. Low Reynolds Number Hydrodynamics. Kluwer Academic Publishers, Norwell, MA.
68. Libai, A., and J. G. Simmonds. 1995. The Nonlinear Theory of Elastic Shells. Cambridge University Press, Cambridge, UK.
69. Salbreux, G., G. Charras, and E. Paluch. 2012. Actin cortex mechanics and cellular morphogenesis. *Trends Cell Biol.* 22:536–545.
70. Clark, A. G., K. Dierkes, and E. K. Paluch. 2013. Monitoring actin cortex thickness in live cells. *Biophys. J.* 105:570–580.